PROCEEDINGS A

royalsocietypublishing.org/journal/rspa

Research

Cite this article: Yadav S, Sagapuram D. 2020 *In situ* analysis of shear bands and boundary layer formation in metals. *Proc. R. Soc. A* **476**: 20190519.
http://dx.doi.org/10.1098/rspa.2019.0519

Received: 12 August 2019
Accepted: 8 January 2020

Subject Areas:
materials sciences, mechanical engineering

Keywords:
shear bands, instability, metals, boundary layer, plasticity

Author for correspondence:
Dinakar Sagapuram
e-mail: dinakar@tamu.edu

Electronic supplementary material is available online at https://doi.org/10.6084/m9.figshare.c.4831875.

THE ROYAL SOCIETY PUBLISHING

In situ analysis of shear bands and boundary layer formation in metals

Shwetabh Yadav[1] and Dinakar Sagapuram[1,2]

[1]Department of Industrial and Systems Engineering, and
[2]Department of Materials Science and Engineering, Texas A&M University, College Station, TX, USA

DS, 0000-0001-9248-5380

Shear banding is a plastic instability in large deformation of solids where the flow becomes concentrated in narrow layers, with broad implications in materials processing applications and dynamic failure of metals. Given the extremely small length and time scales involved, several challenges persist in studying the development of shear bands. Here, we present a new approach to study shear bands at low speeds using low melting point alloys. We use *in situ* imaging to directly capture the essential features of shear banding, including transition from homogeneous to shear banded flow, band nucleation and propagation dynamics, and temporal evolution of the flow around a developing band. High-resolution, time-resolved measurements of the local displacement and velocity profiles during shear band growth are presented. The experiments are complemented by an analysis of the shear band growth as a Bingham fluid flow. It is shown that shear banding occurs only beyond a critical shear stress and is accompanied by a sharp drop in the viscosity by several orders of magnitude, analogous to the yielding transition in yield-stress fluids. Likewise, the displacement field around a nucleated band evolves in a manner that resembles boundary layer formation, with the band thickness scaling with time as a power law.

1. Introduction

Shear banding is a remarkable phenomenon in deformation of solids where the flow becomes spatially concentrated in narrow layers (shear bands) even when the remote loading is homogeneous. Shear banding has been documented in a diverse range of material

systems, including geological materials [1], polymers [2,3] and metals, both crystalline [4,5] and amorphous [6–8]. The occurrence of shear bands in ductile polycrystalline metals has long received particular attention because of their adverse consequences for material failure in processing applications involving large material deformation such as forming [9,10] (also see [11]), machining [12] and wear (tribology) [13]. In addition, shear banding is now recognized as an important mechanism for fracture in high-strain-rate applications such as shock and impact [14,15]; and is also considered as one of the 'hot-spot' ignition mechanisms in powdered and granular explosives [16].

Some distinguishing characteristics of shear bands are their small (but finite) thicknesses in the range of 5–100 μm [17], large plastic strains greater than 10 [18,19], long aspect ratios and unrestrained propagation across microstructural features such as grain or phase boundaries, extremely high strain rates of about 10^5–$10^6\,s^{-1}$ [20], large local temperatures close to melting, and high propagation speeds up to a kilometre per second [21]. To date, shear bands in metals have been studied almost exclusively through post-mortem techniques, with only a few *in situ* observations made of the localization process. Notable exceptions in this regard are the shear band displacement measurements in dynamic torsional experiments by Duffy's group [22] and Giovanola [20,23], where high-speed photography was used to measure the distortion of a grid that is inscribed onto the sample surface. Unfortunately, in both cases, the spatial resolution was coarser than the overall shear band thickness. Similarly, high-speed infrared imaging techniques were used [21,24] to measure the temperature distribution across a shear band that was generated by impacting on a pre-notched plate. These types of measurements, particularly involving characterization of the localized plastic flow in and around the band, are of special importance for understanding the post-localization behaviour of shear bands and eventual transition to fracture. For example, in certain metals, the commencement of localization is immediately followed by fracture, while in other instances, the shear band acts as a site for further plastic flow (with strains sometimes exceeding approx. 100 [18]). The underlying reasons for these differences are unclear. Furthermore, since the characteristic shear band strains and strain rates lie well beyond those that are accessibly by ordinary material tests, measurements made in the neighbourhood of a band may also prove useful for understanding the material response under extreme deformation conditions. However, even to date, high-resolution measurements of velocity, displacement and strain profiles in the region of a developing shear band are scarce, mainly because of the experimental difficulties associated with the very small length (μm) and time (μs) scales involved.

Recently, a micro-marker method has been developed by Sagapuram *et al.* [19,25] to measure shear band displacement and strain fields at high resolution (submicrometre) and under strain rates up to $10^5\,s^{-1}$. The kinematic field data from this technique were further used to deduce the local constitutive response of the shear band. The material in the vicinity of the band was shown to exhibit boundary layer characteristics of a Bingham fluid. While this method has enabled detailed spatial characterization of the boundary layer structure and local material constants (dynamic viscosity), and also appears to be applicable to a variety of metals, being an *ex situ* technique, it is not capable of resolving the temporal dynamics of shear band boundary layer formation.

Here, we introduce a new approach to study shear band formation *in situ* using low melting fusible alloys that have melting points in the range of 50–150°C. A remarkable characteristic of these alloys is that they show similar plastic flow properties to those of conventional (high-temperature) structural metals, while exhibiting shear banding at low strain rates of approximately $10\,s^{-1}$. In prior work [26,27], this has enabled us to capture key details of shear band nucleation, namely, the initiation location, nucleation stress and propagation velocity. In the present paper, we study the post-nucleation growth phase of shear banding with specific focus on the temporal evolution of the shear band boundary layer structure. For this, time-resolved displacement and velocity measurements in the vicinity of a developing shear band are made at high spatial resolution of approximately 1 μm. These observations are complemented by force measurements and a viscous sliding model for the shear band growth so as to analyse the local behaviour of the shear band as a function of the external (imposed) strain rate. Our studies reveal that shear banding occurs only beyond a critical shear stress and is accompanied by a large drop

in the material viscosity, in a manner analogous to the 'solid-to-liquid' phase transition in yield-stress fluids. Our experiments also provide a mechanistic explanation for widening of the shear band thickness, previously conjectured in rate-dependent solids using boundary layer analysis [28,29].

2. Experimental set-up

(a) Shear loading configuration

Two-dimensional plane-strain cutting as shown in figure 1*a* was used as an experimental framework to impose controlled shear deformation under different strain rates. In this geometry, a thin layer of material of predefined thickness t_0 is removed in the form of a chip by shearing action of a sharp wedge-shaped tool. A unique aspect of the cutting geometry is that shear deformation is imposed in a well-characterized and confined zone (red shaded area, figure 1*a*). The average strain rate within the zone can be approximated as $\varepsilon V_0/\Delta$ [30], where V_0 is the relative velocity of sample with respect to tool, ε is the effective (von Mises) strain imposed in the chip and Δ is the shear zone thickness (typically 50–100 µm). This scaling enables a study of shear behaviour of metals over a range of strain rates by simple variation of V_0. Since strains in cutting of ductile metals are typically in the range of 0.5–5 [30], strain rates from 1 to $10^5\ s^{-1}$ are easily accessible by cutting [19,31]. Furthermore, from the standpoint of studying shear bands, an inherent advantage of cutting when compared to some other deformation geometries (e.g. ballistic impact or radial collapse of thick cylinders) is that the evolution of a single shear band can be studied in isolation without interfering effects from the other bands, since only one shear band is active at any given time instant [31].

In our experimental set-up (figure 1*b*), the metal sample is in the form of a rectangular plate ($75 \times 25 \times 2$ mm) that is moved with respect to a stationary tool using a linear slide at a controlled velocity V_0. A ground high-speed steel wedge-shaped tool (edge radius <10 µm and average surface roughness of 0.45 µm) was used as the cutting tool. t_0 was kept constant at approximately 250 µm; this t_0, which is much smaller than the sample width (2 mm), was chosen to ensure plane-strain deformation conditions. The tool rake angle α (figure 1*a*) was varied from 0° to $+40^\circ$. V_0 was in the range of 0.01 to 10 mm s^{-1}. Under cutting conditions where shear banding occurred, we observed that periodic undulations of approximately 3 µm develop on the machined surface. In such cases, before proceeding to the next cut, the surface of the sample was brought back to its original condition (average surface roughness of 1 µm) by making a series of very thin cuts at slow speeds.

The cutting forces in two orthogonal directions (along and perpendicular to V_0) were measured using a piezoelectric dynamometer (Kistler 9129AA, 3.5 kHz natural frequency), mounted directly below the cutting tool (figure 1*b*). The plastic flow and shear band formation were observed *in situ* using a high-speed CMOS camera (pco dimax HS4), coupled with an optical microscope with a $10\times$ objective. To prevent out-of-plane flow and ensure plane-strain deformation at the surface that is being imaged, the side surface of the workpiece was lightly constrained using a sapphire glass plate. Although the camera is capable of recording image sequences at up to 50 000 frames per second, in the present study, frame rates of about 100–2000 per second (depending on V_0) were found to be adequate for capturing the shear band evolution. The spatial resolution of our imaging was 0.98 µm per pixel.

(b) Material system

The material studied is a low melting point bismuth-based alloy, commonly known as Wood's metal, with a nominal composition of 50% Bi, 26.7% Pb, 13.3% Sn and 10% Cd (by weight) and a melting point of 70°C. The material was obtained in an ingot form from RotoMetals Inc. (San Leandro, California). Measurements of thermophysical properties (thermal conductivity, thermal diffusivity and specific heat) of this material were made at Thermophysical Properties Research

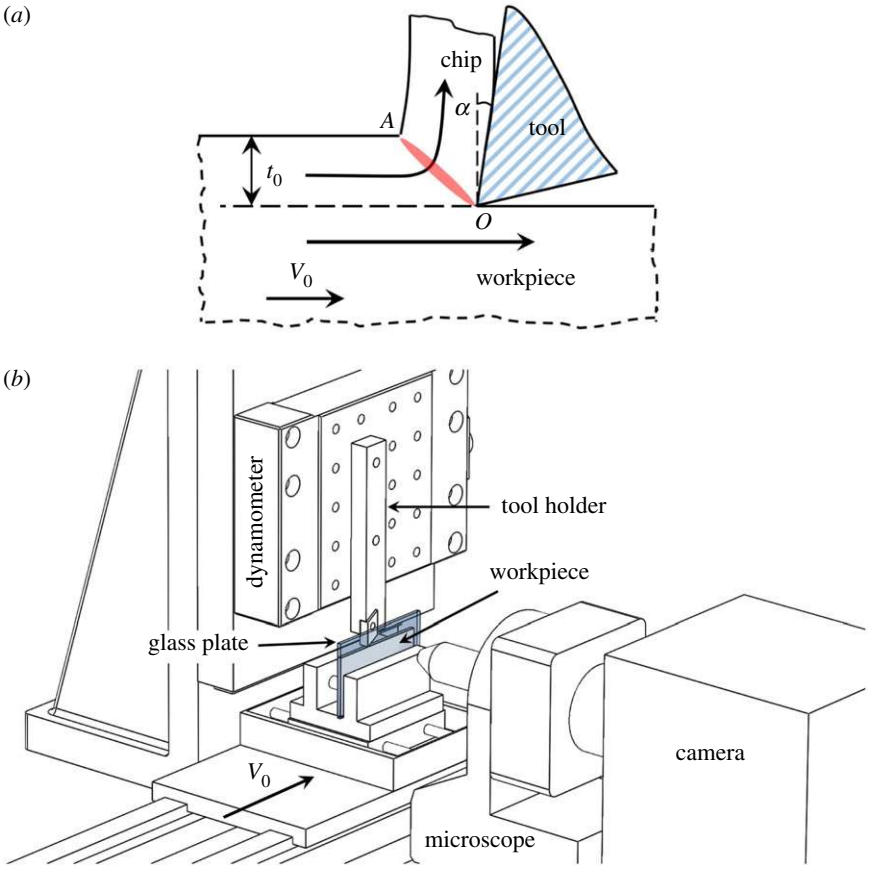

Figure 1. (*a*) Schematic illustrating shear deformation in a two-dimensional plane-strain cutting process. The deformation zone (*OA*) where plastic shearing occurs is highlighted in red. (*b*) Schematic of the experimental set-up used for *in situ* imaging of shear bands and plastic flow. (Online version in colour.)

Table 1. Thermophysical properties of Wood's metal at 23°C.

composition (wt %)	50% Bi, 26.7% Pb, 13.3% Sn, 10% Cd
melting point (T_m)	70°C
density (ρ)	9.26×10^3 kg m^{-3}
thermal diffusivity (κ)	0.14×10^{-4} m^2 s^{-1}
specific heat (C)	165.7 W s kg^{-1} K^{-1}
thermal conductivity (k)	21.5 W m^{-1} K^{-1}

Laboratory Inc. (West Lafayette, Indiana). The room-temperature (23°C) properties are listed in table 1. The thermal diffusivity (κ) was measured using the laser flash technique (ASTM E1461), while the specific heat (C) was measured using a standard differential scanning calorimeter (Perkin-Elmer, ASTM E1269). Bulk density (ρ) was calculated from the sample geometry and mass, and thermal conductivity (k) taken as the product of κ, ρ and C.

Compression tests were carried out initially to evaluate the plastic flow behaviour of this alloy under quasi-static conditions. For this, cylindrical samples of 10 mm diameter and 20 mm height were prepared by first heating the metal to 200°C and slowly pouring the molten metal into

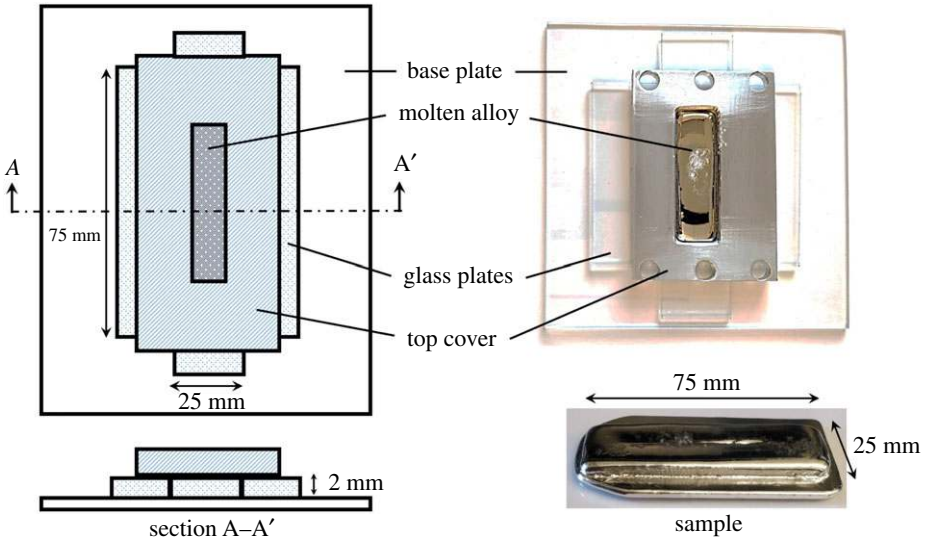

Figure 2. Schematic and a picture illustrating the casting set-up used for sample preparation. The sample was prepared by pouring the molten metal (heated to 200°C) into the 75 × 25 mm slot bounded by the four glass plates. The metal was left to solidify under ambient conditions. (Online version in colour.)

glass cylindrical test tubes with a diameter that is slightly larger than 10 mm. After solidification, the metal was extracted by breaking the test tube and machined on a lathe to the final desired dimensions. For cutting experiments, rectangular plate specimens were prepared using the casting set-up shown in figure 2. A glass plate was used as a base plate and four 2 mm thick rectangular glass plates were used to create a rectangular boundary of 75 × 25 mm. A rectangular aluminium plate with a machined slot was used as top cover through which the molten metal was poured slowly and allowed to spread uniformly in the rectangular region surrounded by the four glass plates. The metal was left to solidify by air cooling, after which the top cover and the glass plates were removed to retrieve the final sample. Both the above casting techniques resulted in samples without any bulk or microscopic porosity. Multiple compression and cutting tests were also carried out to confirm the consistency and repeatability of results from sample to sample.

(c) Time-resolved characterization of shear band displacement profiles

The evolution of deformation field around a shear band was characterized both qualitatively and quantitatively in terms of streaklines, displacements, velocity and strain by analysing the recorded image sequences using an image correlation method, particle image velocimetry (PIV) [32]. PIV is predominantly used in fluid mechanics where particles (markers) injected into the fluid are tracked at different time instances to yield spatial displacement or velocity distributions that characterize the fluid flow [33]. In the current study, the surface roughness features, deliberately introduced onto the side surface of the workpiece, played the equivalent role of markers. In PIV, the displacements are computed by first overlapping an artificial grid on the images and choosing an interrogation window surrounding the grid point. Then, for each grid point, cross correlation is performed between the interrogation window of consecutive images. If $f(i,j)$ and $g(i,j)$ represent the interrogation windows corresponding to the first and second image, respectively, the cross correlation between the interrogation windows is given by

$$f * g(x,y) = \sum_i \sum_j f(i,j) \times g(i+x, j+y), \tag{2.1}$$

where x and y are the displacements of the interrogation window $g(i,j)$ with respect to $f(i,j)$. The displacement of the interrogation window $g(i,j)$ corresponding to the maximum value of cross correlation gives the displacement vector at the grid point under consideration. Similar analysis on all the grid points in an image yields a displacement field map. The other deformation parameters such as velocity, strain rate and strain are then determined using the displacement data. The velocity field (u,v) results directly from the displacement field information and the time interval between consecutive images, whereas the strain rate is evaluated from spatial differentiation of the velocity field as

$$\dot{\varepsilon}_{xx} = \frac{\partial u}{\partial x}, \quad \dot{\varepsilon}_{yy} = \frac{\partial v}{\partial y}, \quad \dot{\gamma} = 2\dot{\varepsilon}_{xy} = \frac{\partial v}{\partial x} + \frac{\partial u}{\partial y}$$

and

$$\dot{\varepsilon} = \sqrt{\frac{4}{9}\left(\frac{1}{2}\left[(\dot{\varepsilon}_{xx} - \dot{\varepsilon}_{yy})^2 + \dot{\varepsilon}_{xx}^2 + \dot{\varepsilon}_{yy}^2\right] + \frac{3}{4}\dot{\gamma}^2\right)}, \tag{2.2}$$

where $\dot{\varepsilon}$ is the effective plastic strain rate. The plastic strain field is then calculated by integrating the strain rate field as a path integral from the start until the end of the experiment.

3. Results

The *in situ* study of the plastic flow during cutting using imaging has provided insights into transition from the homogeneous to shear banded flow as well as temporal dynamics of the localized flow near the band, post the instability onset. The observations suggest that band formation occurs when the shear (flow) stress attains a critical value, while the dynamics of the shear band boundary layer growth is determined by the local viscosity parameter.

(a) Plastic flow behaviour of Wood's metal

The initial set of experiments have focused on understanding the overall plastic flow behaviour of the Wood's metal using compression tests (ASTM E9-09). The tests were carried out under different compression speeds between 0.001 and 1.0 mm s^{-1}; the corresponding (nominal) strain rates were in the range of 10^{-5}–10^{-2} s^{-1}. An oil-based lubricant (petroleum jelly) was used to minimize the friction between the sample and compression platens. No significant barrelling was observed up to strains of about 0.6. The representative true stress–strain curves at different strain rates are shown in figure 3*a*. The material is seen to exhibit a slight amount of softening immediately after yielding, followed by flow stress saturation beyond strains of approximately 0.3. This strain-softening behaviour is most likely a consequence of the material's low melting point. In this regard, it may be noted that the room temperature at which the tests were conducted corresponds to a high homologous temperature ($T_H = T(\mathrm{K})/T_m(\mathrm{K})$) of 0.86. From the figure, it is also evident that the material is highly rate sensitive. Figure 3*b* illustrates the rate dependence where the yield stress (σ_y) is plotted against the strain rate ($\dot{\varepsilon}$) on a logarithmic scale. The linear plot suggests that the material can be described using a constitutive law of the form: $\sigma = K\dot{\varepsilon}^m$, with m being the strain rate sensitivity. Similar analysis at different strain levels showed that m falls in the range of 0.13–0.17. It should be noted that the above equation which ignores strain and temperature dependence is a simplified form of the full constitutive law. As will be shown in the subsequent sections, the plastic strains at which shear bands typically initiate are $\gtrsim$0.5, with the strains within the band themselves being an order of magnitude higher. Given that the temperature rise in our low-speed cutting experiments is no more than a few degrees Celsius (e.g. see discussion in §4a and also table 2), and considering that the flow stress is independent of the strain at strains $\geq$0.3 (figure 3*a*), the above power-law equation provides a good description of material flow behaviour under large strain conditions of particular interest to this study.

It should be also noted that this type of 'purely' rate-dependent material behaviour (i.e. with little dependence on strain) is prototypical of regular high-temperature metals ($T_m > 600^\circ$C)

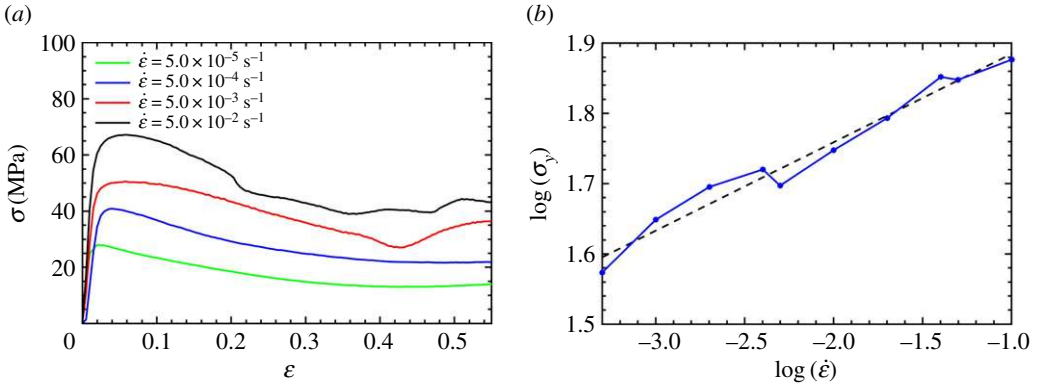

Figure 3. Plastic flow behaviour of the Wood's metal. (*a*) True stress–strain curves from the compression tests carried out at room temperature under different strain rates. (*b*) Logarithmic plot showing yield stress (σ_y) dependence on the strain rate ($\dot{\varepsilon}$). (Online version in colour.)

Table 2. τ data at different V_0 ($\alpha = 0^\circ$). For $V_0 \geq 0.4$ mm s^{-1} (shear banding regime), τ corresponds to the critical shear stress τ_C at band formation, calculated from equation (3.1). For each V_0 condition, the mean and one standard deviation values reported come from 100+ bands. For $V_0 < 0.4$ mm s^{-1} (homogeneous flow), τ represents the average shear flow stress of the material. $\Delta\theta$ is the temperature rise at the onset of band formation, estimated using equation (4.1).

V_0 (mm s^{-1})	0.01	0.05	0.1	0.4	0.6	0.8	1.0	4.0	8.0
τ (MPa)	52.62	54.15	57.11	72.52	66.72	67.76	68.58	74.10	78.27
±1 s.d.	±2.4	±2.3	±2.5	±2.0	±1.8	±4.2	±2.5	±2.4	±2.7
$\Delta\theta$ (°C)				0.16	0.24	0.31	0.39	1.5	2.8

under high strain rates $>10^4$ s^{-1}; for example, see high-strain-rate data for Al, Cu, iron and steels in [34,35]. Furthermore, the near-adiabatic (plastic) heating in high-strain-rate deformation may be expected to result in high homologous temperatures ($T_H \sim 0.6$–0.9), similar to that in the present case. Therefore, we regard the low melting point Wood's metal as a 'model' system for replicating all the essential features of high-strain-rate behaviour of metals, including shear banding, as will be shown below.

(b) Transition from homogeneous to shear banded flow

An exploration of the cutting behaviour of Wood's metal under different V_0 and α revealed primarily two modes of plastic flow—homogeneous flow and shear localized flow—with a flow transition occurring between the two upon increasing V_0. Figure 4 shows this transition with V_0 at $\alpha = 0^\circ$. The PIV-measured effective strain field (ε) and streaklines (white lines), superimposed on the raw images, are shown. At $V_0 = 0.01$ mm s^{-1} (figure 4*a*), the flow is homogeneous as can be seen from the smooth streaklines and relatively uniform deformation in the chip. This type of flow results from uniform shear in the deformation zone, and has been the basis for most of the theoretical analyses of cutting. By contrast, at a higher V_0 of 0.6 mm s^{-1} (consequently, higher strain rate), the flow in the chip is separated into two distinct regions: macroscopic shear bands with high strains of approximately 4 and the low-strain regions ($\varepsilon < 1$) in between the bands (figure 4*b*). The 'serrated' chip morphology and streaklines in figure 4*b* also reveal the periodic localization of shear within the bands and an undulating flow pattern that is distinctly different from that in figure 4*a*. Figure 4*c*,*d* shows the corresponding force traces, with F_C and F_T being the force components along and perpendicular to the V_0 direction, respectively. Clearly, the

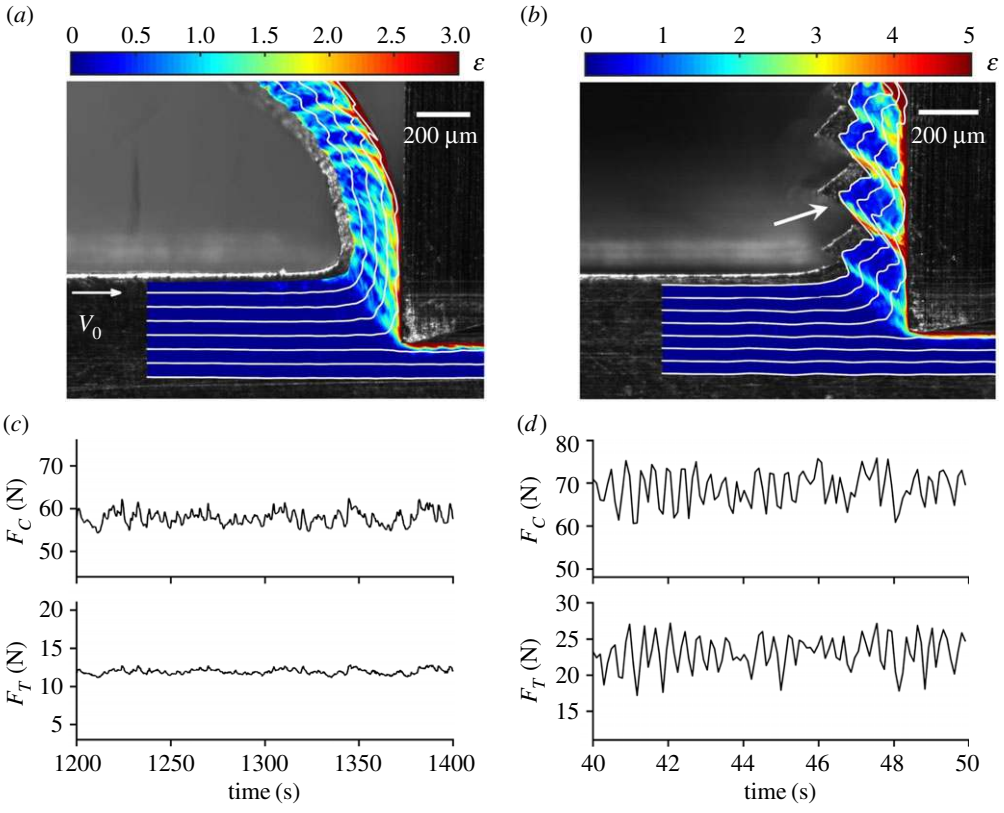

Figure 4. PIV (von Mises) plastic strain field (ε) and streaklines showing the transition from homogeneous to shear banded plastic flow with increasing V_0. (*a*) Laminar plastic flow at $V_0 = 0.01\,\mathrm{mm\,s^{-1}}$ characterized by the uniform strain field and smoothly varying streaklines. (*b*) Shear banding at $V_0 = 0.6\,\mathrm{mm\,s^{-1}}$, exhibiting periodic flow localization along well-defined macroscopic shear bands separated by low-strain regions. The 'serrated' morphology of the chip free surface is marked using an arrow. The corresponding cutting forces, F_C and F_T along and perpendicular to V_0 direction, respectively, are shown in (*c*) and (*d*). (Online version in colour.)

forces are quite steady and exhibit little variation in the homogeneous flow case. On the other hand, the shear banded flow exhibits strong periodic oscillations, with each force oscillation corresponding to individual band formation. The development of both these flow types is also shown in electronic supplementary material, videos S1 ($0.01\,\mathrm{mm\,s^{-1}}$) and S2 ($0.6\,\mathrm{mm\,s^{-1}}$).

At this point, it is worthwhile to distinguish the small-scale heterogeneities in the strain field seen in the homogeneous flow case (figure 4*a*) from the macroscopic shear bands. An important distinction is that the small strain heterogeneities do not traverse throughout the width of the sample (chip), whereas shear bands do. This is illustrated using figure 5 which shows the topography plots taken from the free surface of the chips using a three-dimensional optical profilometer. The chip flow direction (V_C) is also shown using an arrow in figure 5 for reference. The free surface of the chip produced via homogeneous flow (figure 5*a*) is seen to be relatively flat, albeit with some small undulations that are scattered randomly on the surface. By contrast, clear surface shear steps about 170 µm deep, traversing the entire chip width, can be seen in figure 5*b*. These surface steps directly correspond to the 'serrations' seen on the free surface of the chip, when viewed from the side angle; for example, see at arrow in figure 4*b*. As will be shown in the following section, these shear steps on the surface arise directly as a result of (periodic) localized shearing within the shear band during its growth phase. The focus here will be on macroscopic shear band structures such as in figures 4*b* and 5*b*.

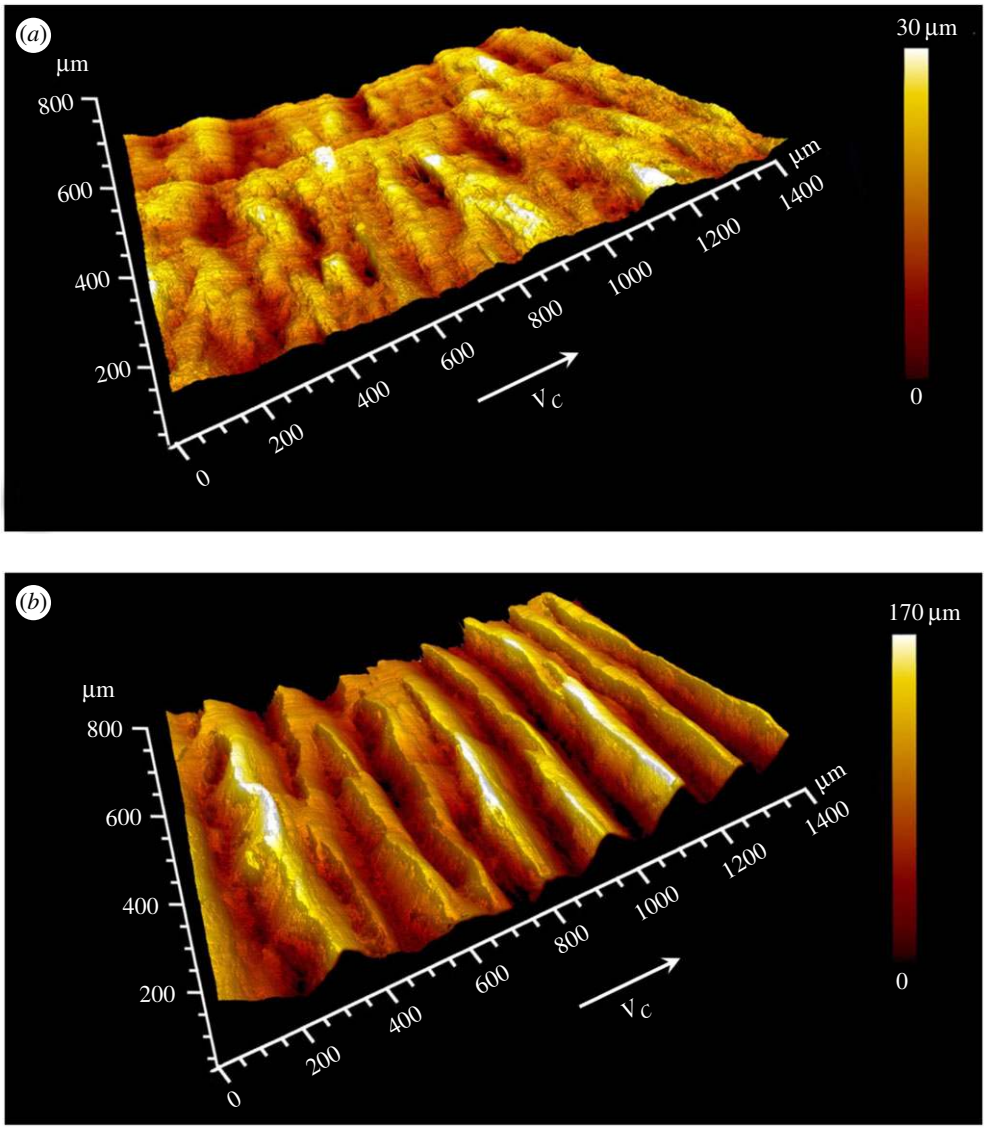

Figure 5. Free surface topography plots of chips produced under (*a*) homogeneous flow ($V_0 = 0.01$ mm s^{-1}) and (*b*) shear banded flow ($V_0 = 0.6$ mm s^{-1}) conditions. Well-defined shear steps, traversing the chip width, are seen in the shear banding case, whereas the homogeneous flow case is characterized by small-scale surface undulations. Note that the shear steps seen in (*b*) directly correspond to the serrations on the free surface of the chip shown earlier in figure 4(*b*). The direction of chip velocity (V_C) is shown for reference. (Online version in colour.)

It should be also noted that the above transition from homogeneous flow to shear banding with increasing strain rate is well known in the engineering literature under different loading configurations, including torsion [20,22], machining [12,31,36], punching [4] and impact [17]. However, in conventional high-temperature metals, this transition occurs only at high strain rates beyond 10^4 or 10^5 s^{-1}. That the low melting point Wood's metal reproduces the exact same flow transition at strain rates multiple orders lower in magnitude is noteworthy. Coupled with the fact that its room temperature quasi-static flow behaviour resembles the high-strain-rate behaviour of structural metals, this enables us to study shear band phenomena at slow speeds without being burdened by the experimental challenges.

(c) Shear band nucleation and growth

Figure 6*a* is a high-speed image sequence (with superimposed strain field) showing different stages involved in the formation of a single shear band at $V_0 = 1.0\,\mathrm{mm\,s^{-1}}$ ($\alpha = 0^\circ$). The corresponding oscillatory force profiles are shown in figure 6*b* with points A–I on the plot directly corresponding to the time instances of frames A–I in figure 6*a*. The time marked in figure 6*a* corresponds to the time elapsed after the termination of a previous shear band. In frames A–C, the smooth streaklines represent a stable flow which occurs under a steadily rising load. The instability in the flow occurs in frame D, triggered by nucleation of a shear band at the tool tip, which is seen as a pocket of high strain (see at arrow). The strain front, which is also the shear band front, then propagates towards the free surface of the sample, reaching it in frame F. It may be noted that the propagation of the band front is also accompanied by progressive formation of 'kinks' in the streaklines, indicating the local deformation is that of shear. We refer to this phase shown by frames D–F as the band nucleation, for it is during this phase that a well-defined shear band plane PQ is fully established. The orientation of this shear band plane, inclined at approximately 40° with respect to V_0, is consistent with the plane of maximum shear stress. Tracking of the band front during the nucleation phase shows that it propagates at a constant velocity. For example, see figure 7 where the blue points represent the distance traversed by the band front at different time instances, with respect to the tool tip (band initiation location). Of the five points shown in figure 7, three correspond to frames D–F shown in figure 6*a*, where the band front location is shown using an arrow. A linear plot with time reveals a nearly constant propagation velocity (V_N) of $4.3\,\mathrm{mm\,s^{-1}}$.

Frames G–I in figure 6*a* represent the subsequent growth (or sliding) phase of shear banding. This phase is characterized by localized sliding of the material along the band plane PQ under a falling load, as if the material in the immediate vicinity of the band has lost its resistance to flow and material blocks on either side of the band begin to 'slip' as rigid bodies. From figure 6*b*, it is seen that the onset of sliding coincides with the maximum in the force trace.[1] It is also evident that the shear step at the free surface and intense localized strains in the vicinity of the band predominantly develop during this sliding process. To illustrate the shear step formation at the surface, two surface points Q and R that are initially right adjacent to each other before the sliding phase are marked in frame F. In frames G–I, these two points are seen to get displaced with respect to each other, and thus forming a shear step QR, as a result of localized sliding between the low-strain segments on either side of the shear band. The serrated surface morphology shown earlier in figures 4*b* and 5*b* arises as a consequence of periodic events involving band nucleation and sliding. That the shear steps resulting from sliding traverse across the width of the sample can be also seen from figure 5*b*.

The sliding velocity characteristics during the band growth can be inferred from figure 7, where the red points represent the shear step distance at the free surface, QR (frames G–I, figure 6*a*), as a function of time. Again, the linear plot suggests that sliding occurs at a constant sliding velocity (V_S) of $1.2\,\mathrm{mm\,s^{-1}}$. This value is in fact very close to the resolved component of the cutting velocity V_0 along the band, approximately $1.5\,\mathrm{mm\,s^{-1}}$. In a prior study [27], V_N was shown to be a constant independent of V_0, while V_S varies proportionally with V_0. After a finite time (approx. 150 ms after the onset of sliding), the sliding process is terminated and deformation switches to the neighbouring region, at which point, the load rises again. The phenomenological details of shear band formation in the current material system, namely, band nucleation at the tool tip, propagation towards the free surface and subsequent sliding, are in agreement with that observed in other systems such as titanium [31].

(d) Characteristic stress for shear band formation

The fact that macroscopic sliding at the shear band always commences when the cutting force F_C reaches a maximum enables us to define a characteristic stress (τ_C) for the onset of shear band

[1]Observations of several other bands showed that the commencement of sliding strictly coincides with the maximum in F_C, but not necessarily F_T.

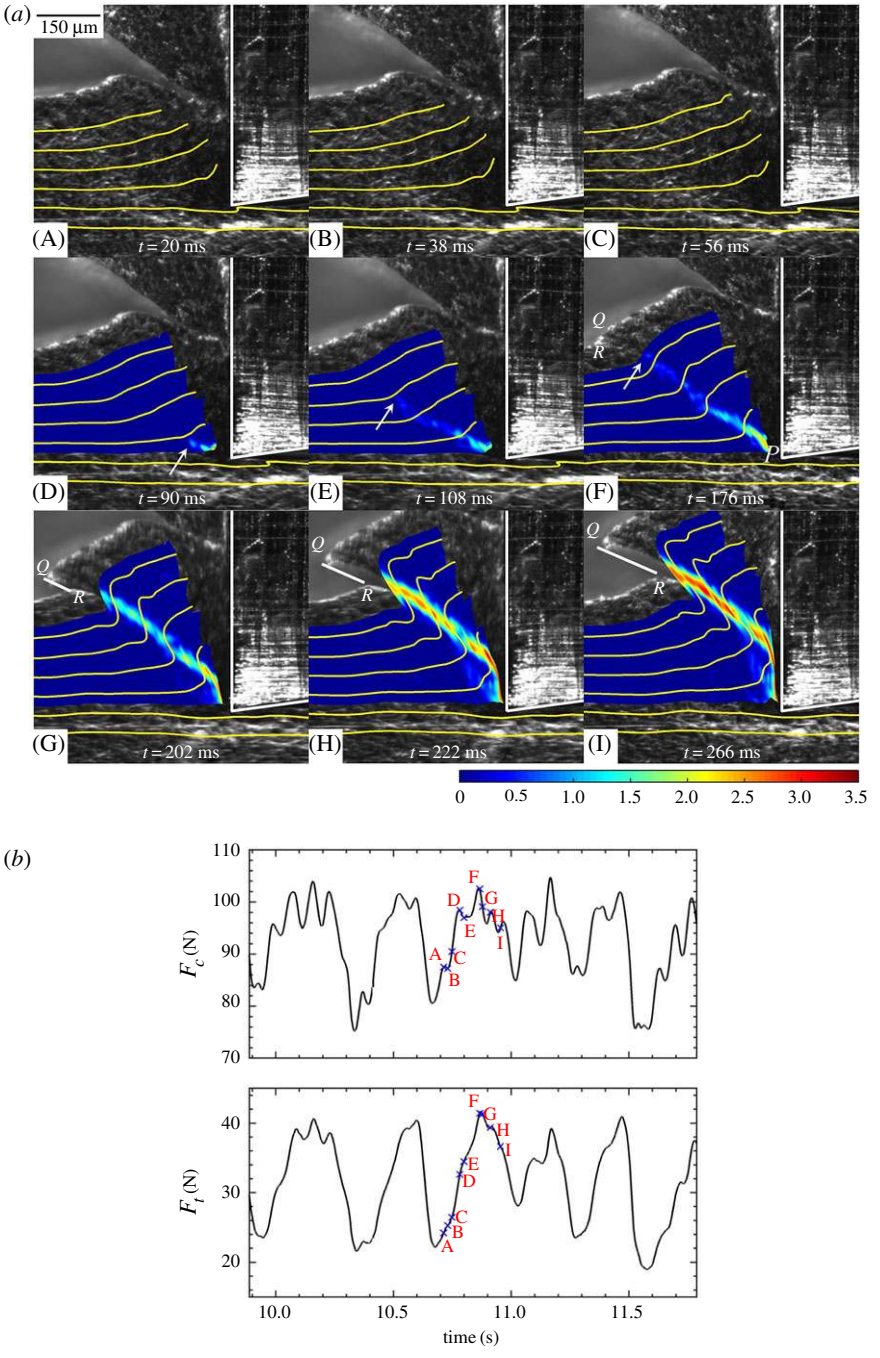

Figure 6. Dynamics of single shear band formation. (*a*) High-speed images (with superimposed streaklines and plastic strain field) showing single shear band formation at $V_0 = 1.0$ mm s^{-1}. The plot in (*b*) shows oscillatory force profiles during shear banding, with each oscillation corresponding to the formation of a single shear band. The points A–I marked on the force profiles correspond to the exact time instances of frames A–I shown in (*a*). The first three frames (A–C) show the formation of low-strain region adjoining the shear bands. The shear band nucleation occurs near the tool tip in frame D, followed by propagation towards the free surface (the band front location is marked by a white arrow for reference). In frame F, the band has just reached the surface, with the load being maximum at this instant. Frames G–I show the subsequent stage which is characterized by macroscopic sliding along the shear band. This slip accounts for most of the strain localization around the band. The shear step at the free surface, *QR* (see frames G–I), is also developed during this sliding stage. (Online version in colour.)

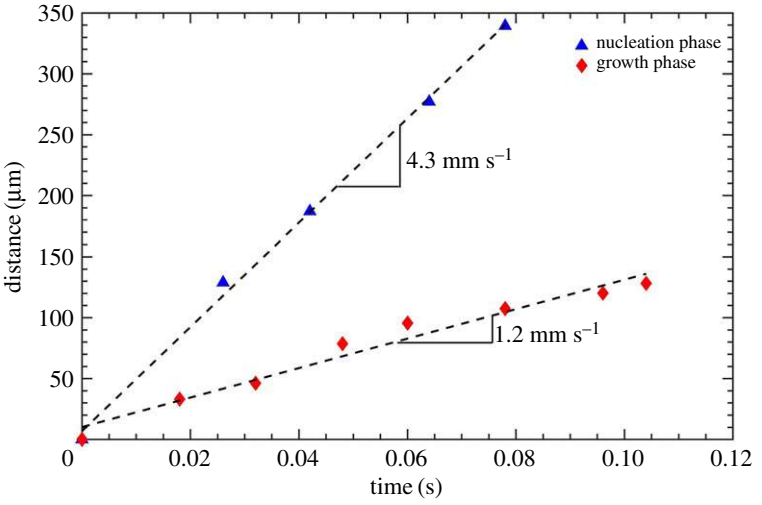

Figure 7. Plot showing the shear band velocity characteristics during nucleation and growth phases. Blue points represent the distance between the band front and the tool tip during nucleation (frames D–F, figure 6*a*), while red points correspond to the length of the shear step at the free surface (marked by *QR* in frames G–I, figure 6*a*) resulting from sliding. The linear plots suggest a constant band propagation (4.3 mm s^{-1}) and sliding velocity (1.2 mm s^{-1}). $V_0 = 1$ mm s^{-1}. (Online version in colour.)

growth. τ_C is simply the shear force along the band plane PQ, at the instant when F_C reaches maximum, divided by the plane area. Our experiments showed that at $\alpha = 0^\circ$, both F_C and F_T reach their maximum nearly at the same time instant, while this is not necessarily true for other α. Therefore, for the present case ($\alpha = 0^\circ$), τ_C is given by

$$\tau_C = \frac{F_{C\max} \sin\phi \cos\phi - F_{T\max} \sin^2\phi}{(b \times t_0)}, \tag{3.1}$$

where $F_{C\max}$ and $F_{T\max}$ are the peak cutting and thrust forces, respectively, ϕ is the shear band angle (with respect to V_0), and b is the sample width.

This yields a value for τ_C of about 70 MPa for the shear band discussed in figure 6, which is nearly twice that of the shear yield stress of the material (figure 3). τ_C calculations for several other bands at the same V_0 have shown that its variation from band to band is quite small. For example, figure 8*a* shows the τ_C data for 125 bands, gathered from a single cutting experiment. Maximum variation in τ_C is seen to be less than 10%. Figure 8*b* is the frequency distribution plot showing that τ_C follows a normal distribution, with a mean and standard deviation of 68.6 MPa and 2.5 MPa, respectively. Henceforth, mean values are used to represent τ_C for any given experimental condition.

Interestingly, experiments at different V_0 showed that τ_C is independent of the imposed deformation rate (V_0). Table 2 shows τ_C data for shear bands formed under different V_0 conditions, varying over one order of magnitude (0.4–8 mm s^{-1}).[2] τ_C is seen to be essentially constant, at about 70 MPa, suggesting a critical shear stress-type criterion ($\tau = \tau_C$) for band formation. This in fact explains the steady-state homogeneous flow at lower V_0. For instance, for the homogeneous flow case, the material's shear flow stress during cutting may be estimated again from equation (3.1) by replacing $F_{C\max}$ and $F_{T\max}$ with the average steady-state forces, and ϕ with the nominal shear zone angle. The shear flow stress values thus estimated for $V_0 \leq 0.1$ mm s^{-1} are also given in table 2. At these low V_0 conditions, the shear flow stress is clearly seen to be lower than the critical stress τ_C, which explains the homogeneous nature of the flow observed at these speeds.

[2] V_0 above 10 mm s^{-1} resulted in completely fragmented chips, as opposed to continuous shear banded chips.

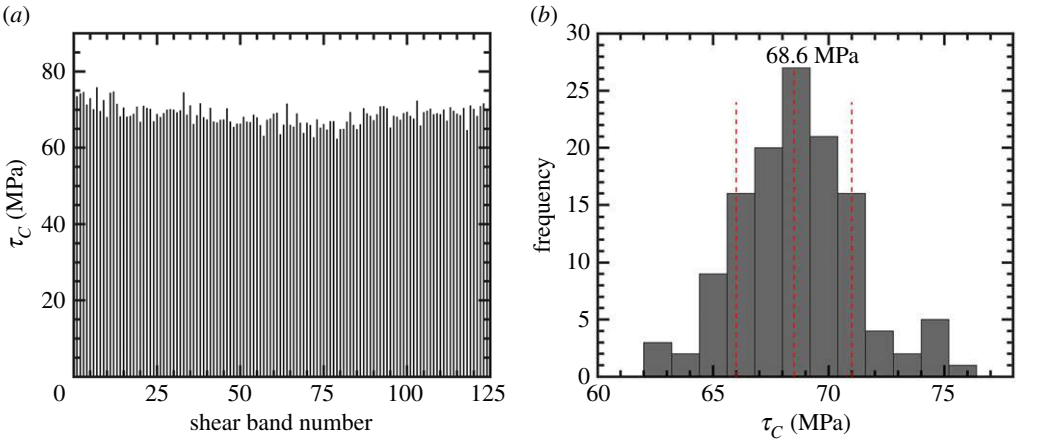

Figure 8. (*a*) Critical shear stress (τ_C) data for 125 shear bands formed at $V_0 = 1$ mm s^{-1}. The stress values fluctuate around 70 MPa, with less than 10% variation. (*b*) Frequency distribution plot of τ_C for the same dataset, showing that the data are normally distributed. The mean (68.6 MPa) and standard deviation (2.5 MPa) are marked by red dashed lines. (Online version in colour.)

We also studied the effect of loading geometry by changing the tool angle α and found that τ_C is insensitive (within experimental uncertainty) even to α, suggesting that it is a physical characteristic of the material. However, the critical V_0 at which shear banding first occurs was found to increase with increasing α (more positive). Taken together, these experimental observations suggest that the material around a nucleated band exhibits macroscopic slip when the stress across that plane reaches a critical value.

(e) Spatio-temporal evolution of plastic flow during shear band growth

Spatio-temporal evolution of the flow adjacent to the band, post shear band nucleation, is studied quantitatively using *in situ* imaging and PIV analysis. For this, a streakline passing roughly through the centre of the chip was tracked at different time instances of the shear banding process. Figure 9 depicts the evolution of such a streakline ($V_0 = 0.6$ mm s^{-1}), where the streakline position after every 2.5 ms is shown. The darkest line corresponds to the time instant when the shear band front has just reached the streakline (band nucleation phase), with the lightest shade corresponding to the end of the shear band growth phase. The shear band centre, which is the intersection point of the band front with the streakline, is also marked using a red asterisk for reference. It should be noted that the locus of these points is a pathline, and thus represents the general motion of the shear band centre plane in Eulerian space.

Figure 10*a* shows the time evolution of effective strain along two different streaklines (1 and 2) located at a distance of 280 and 115 µm from the tool tip. Relative positions of streaklines 1 and 2 with respect to the tool and workpiece/chip free surface are shown in figure 10*b* for reference. Here, x is oriented along the length of the shear band, with $x = 0$ corresponding to the tool tip. The other axis y is perpendicular to the shear band plane. In figure 10*a*, strain is plotted against perpendicular distance from the band centre (which is represented by $y = 0$) at different times (t) of the shear banding process, with $t = 0$ corresponding to the shear band nucleation stage. At $t \approx 0$, the strain profile in figure 10*a* is seen to be relatively flat. With increasing t, the strain localization around the band is seen to evolve like a diffusion growth process, that is to say not only the maximum strain at $y = 0$ grows with time, but also the localized strain 'spreads' laterally in y. Note also that the strain field evolves symmetrically around the shear band plane.

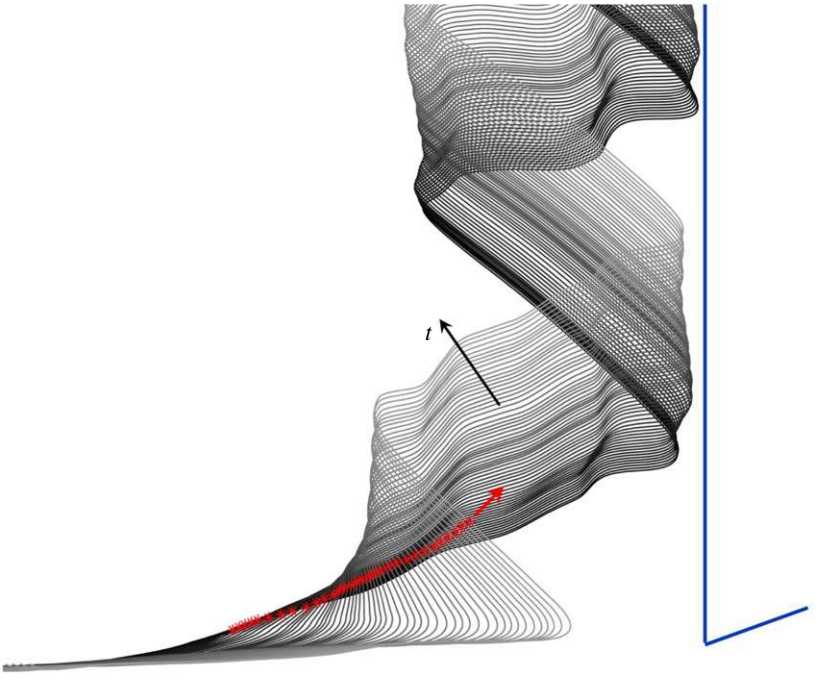

Figure 9. Time evolution of a streakline passing through the centre of a shear band ($V_0 = 0.6$ mm s^{-1}). Each curve represents new shape and position (with respect to stationary tool) of the streakline after every 2.5 ms. The 'intersection' point of the streakline with the band is marked by red asterisks, whose locus represents the pathline of the shear band plane. The streakline with the darkest shade corresponds to the start of the growth phase, while and the lightest shade represents the end. (Online version in colour.)

A further detailed analysis of the shear band growth, in terms of the displacement field, is given in figure 11. Given the symmetry, only one side (right half) of the shear band plane is considered here. Here, $U(y,t)$ is the shear displacement at any point along the streakline located at a perpendicular distance y at any time t, with the displacement calculated with respect to the shear band plane frame of reference (red asterisk in figure 9). $U_{\max}(t)$ represents the maximum shear displacement remote from the plane $y = 0$ at any time instance. The displacement field thus obtained is shown as a spatio-temporal diagram in figure 11*a*, where the normalized displacement $U/U_{\max}(y,t)$ in the vicinity of a shear band is colour-coded. The evolution of the displacement profile $U(y)$, as a function of time, is also shown in figure 11*b*. The displacement profiles are immediately seen to evolve in a self-similar manner. At small t ($\approx$0.01 s), the flow is essentially confined to only around the band centre ($y \leq 5\,\mu$m). However, upon sliding (increasing t), the flowing region grows laterally, eventually attaining a width of about 35 μm at the end of the sliding process ($t = 0.2$ s). This lateral growth of shear band can be also seen from the white line in figure 11*a*, which shows the temporal evolution of shear band half-thickness (which we define as the y where $U = 0.99U_{\max}$). This type of shear band growth with time closely resembles the boundary layer growth in viscous fluids, where the layer thickness scales as $t^{1/2}$ [37].

The spatial gradient in the displacement field in the direction along the length of the band is shown in figure 11*c*,*d*, which are snapshots of the normalized displacement field $U/U_{\max}(y,x)$ at a given time instance close to the end of the sliding process. Here, x is a spatial variable that corresponds to the location along the band length, with $x = 0$ coinciding with the tool tip P. One hundred streaklines covering a 170 μm distance across the band length ($x =$ 260–430 μm) were considered in these measurements. Note therefore that each vertical slice in figure 11*c* or each curve in figure 11*d* represents an individual streakline. From figure 11*d*, all the displacement profiles can be seen to be self-similar. The displacement profiles are also seen to be consistently

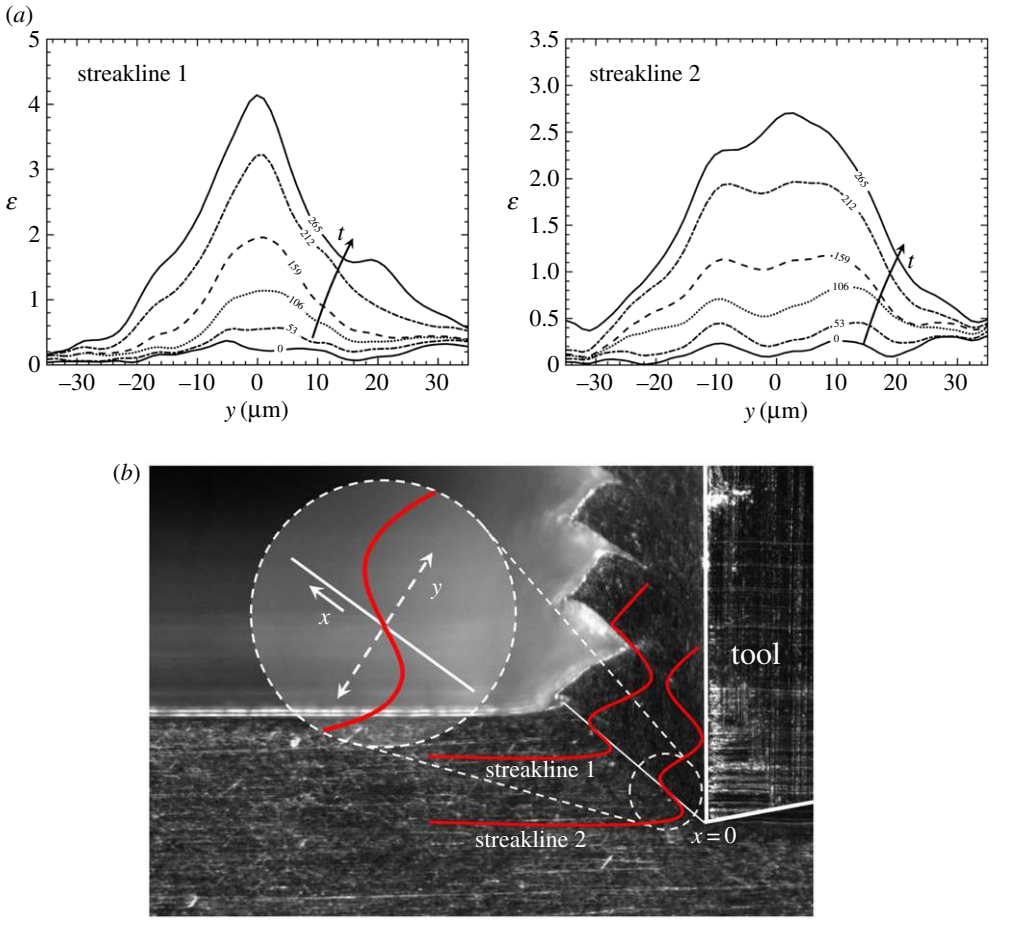

Figure 10. Strain evolution during shear band growth. (*a*) The effective plastic strain around the shear band plane ($y = 0$) plotted at different times. The time shown on the strain profiles is in ms. Data are taken from two different streaklines (1 and 2) from different locations along the band length. The relative positions of these two streaklines are shown in (*b*). An enlarged view of the streakline, shown in (*b*), also illustrates the orientation of *x*- and *y*-axes with respect to the shear band. (Online version in colour.)

more 'diffuse' at smaller x (i.e. streaklines closer to the tool tip). This is likely because of the fact that streaklines close to the tool tip are those that are first intersected by the shear band front, and as a result, at any given time instance, the 'effective' t for these streaklines will be somewhat larger compared with those near the free surface. A simple calculation of the gradients along the length of the shear band (x), however, shows that they are much smaller than those perpendicular to the band plane (along y-direction). The characteristic gradients along x may be obtained by looking at how the band thickness varies along the band length. From figure 11*c*, the effective band thickness, characterized by y where $U/U_{\max} \approx 0.99$, is seen to vary from 40 μm to 20 μm over an x of 170 μm. This yields a gradient of approximately 0.12. On the other hand, the y-gradient, which is simply the ratio of $U_{\max}$ to band thickness, is in the range of 2–5, more than an order of magnitude higher than the x-gradient. This suggests that the shear band structure may be approximated as one dimension.

(f) Bingham model for shear band growth

Complementing the full-field shear band measurements presented in the previous section, we explore a simple analytical model for the shear band growth with a view to understand the local

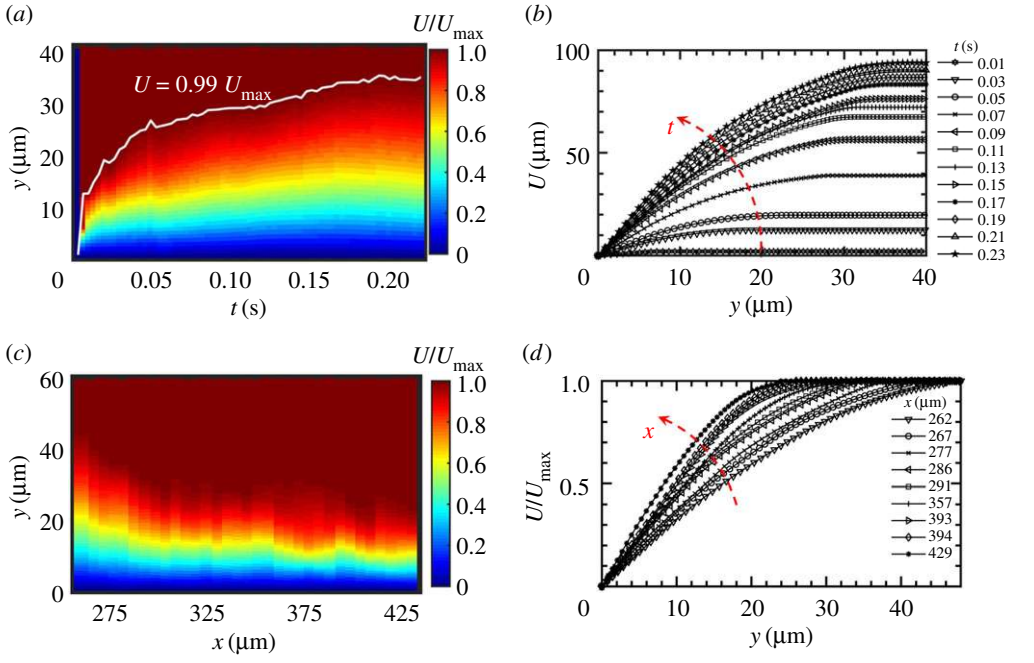

Figure 11. Dynamics of shear band growth. (*a*) Spatio-temporal diagram showing the normalized displacement data (U/U_{max}) around a shear band as a function of the normal distance from the shear band centre (y) and sliding time (t). Also shown in white line is the location of y where $U = 0.99U_{max}$, which can be taken as the shear band thickness. (*b*) Raw shear band displacement data plotted against y at different t. (*c*) Spatial diagram showing U/U_{max} as a function of y and different locations along the length of the band (x), taken at a specific time instant $t = 0.2$ s. (*d*) Normalized displacement data at $t = 0.2$ s plotted against y for different values of x . $V_0 = 0.6$ mm s^{-1}. (Online version in colour.)

constitutive behaviour of the boundary layer material adjacent to the band. Before proceeding with the analysis, a discussion of the role of temperature in band growth is in order. As seen from figure 11, by the end of the growth phase, the shear band attains a characteristic (half) thickness of about 35 μm, which agrees well with the typical shear band thicknesses reported in other material systems [8,17–19]. Traditionally, this length scale has been primarily attributed to thermal diffusion around the shear band centre, with the band thickness associated with the characteristic thermal diffusion length [7,8]. Thermal diffusion around the band may be analysed by assuming the shear band plane to be a stationary planar heat source of constant strength, for which the temperature solution is given by Carslaw & Jaeger [38]. In this case, the characteristic thermal diffusion length, over which approximately 70% of heat is contained at any time instance t, is given by $\sqrt{\kappa t}$. For the present case where $\kappa = 0.14 \times 10^{-4}$ m^2 s^{-1} (table 1) and taking t as the total shear band sliding time (approx. 230 ms at $V_0 = 0.6$ mm s^{-1}), the thermal diffusion length should be about 1.8 mm, which is two orders higher than the observed shear band half-thickness and even larger than the spacing between individual shear bands (see figure 4*b*, for reference). Coupled with the low deformation rates in this study where the band temperature rise is expected to be small (see discussion in §4a), this clearly suggests that thermal diffusion cannot be the main factor governing the shear band growth.

The three observations above, namely lateral growth of shear band thickness with time, slow variation of the flow field along the length of the band, and little contribution of temperature to the band growth, led us to model the shear band flow kinematics as a boundary layer problem, similar to that in our previous study [19]. During the band sliding (growth) phase, we treat the band half-space as a semi-infinite viscous block sliding past a stationary interface located at $y = 0$. Specifically, at $t = 0$ when the band plane is just established, the viscous half-spaces on either side of the band are at rest, and for $t > 0$, they slide with a velocity of $V_S/2$ in opposite directions

with no-slip boundary condition at the interface ($y = 0$). It may be noted that this flow geometry is equivalent to the classical velocity-driven Rayleigh problem. In view of the fact that shear band sliding sets in when the shear stress reaches a critical value τ_C (table 2), coupled with the observation of boundary layer-like flow kinematics during the band growth (figure 11), we also assume that the material in the vicinity of the shear band to be a Bingham fluid with a yield stress τ_C and a constant dynamic viscosity μ. For this flow geometry, in the absence of pressure gradients, the momentum equation is

$$\frac{\partial V(y,t)}{\partial t} = \frac{1}{\rho}\frac{\partial \tau(y,t)}{\partial y}, \tag{3.2}$$

where τ is the shear stress and ρ is the density. By taking the material to be at rest at $t = 0$, and applying the boundary conditions of no-slip at the interface ($V_{y=0} = 0$) and constant remote velocity ($V_{y\gg 0} = V_S/2$) for $t > 0$, the above equation can be solved to arrive at the velocity field $V(y,t)$. Pascal [39] has studied the Rayleigh problem for a generalized Herschel–Bulkley fluid and showed that for an ideal Bingham fluid, the velocity solution converges to that of a Newtonian fluid, while for a shear-thinning fluid, it converges to that of a power-law pseudoplastic fluid. The equivalence between the Bingham fluid and Newtonian fluid in Rayleigh flow has been also discussed by Huilgol [40]. Therefore, for the present case, the velocity equation reduces to the well-known diffusion equation: $V_S/2\mathrm{erf}\,(\xi)$, where $\xi = y/\sqrt{4\nu t}$ is the self-similarity variable and $\nu = \mu/\rho$ is the kinematic viscosity. Time integration of this equation leads to the displacement field $U(y,t)$:

$$\frac{U}{U_{\max}} = -2\xi^2\mathrm{erfc}(\xi) + \mathrm{erf}(\xi) + \frac{2\xi}{\sqrt{\pi}}\exp(-\xi^2). \tag{3.3}$$

From equation (3.3), it is clear that the only variable in the model is the band viscosity (given by μ or ν). Also for a given viscosity, the model correctly predicts the lateral growth of band thickness with time, consistent with the experimental observations (figure 11*a*,*b*). The normalized shear band displacement data from experiments, scaled using the fitting variable ν, are plotted as a function of ξ in figure 12. The individual displacement profiles shown in the figure come from two different streaklines (indicated by black and grey coloured points) and different time instances of the shear banding process. By appropriate selection of ν, all the profiles are seen to cluster together and roughly fall on a single master 'curve', matching with the curve predicted by equation (3.3) (solid blue curve). In view of the approximations made, the agreement between experimental data and the model is surprisingly good. Firstly, this suggests that the shear band growth is indeed (momentum) diffusion dominated which can be described by a Bingham-type rheology. Secondly, this also allows us to back-calculate the local shear band viscosity. The band viscosity μ, as obtained from the fitting variable ν, is shown in the inset to figure 12. It is seen that μ slightly decreases during the initial stages of localization, but remains in a small range of 1–2.5$\times 10^{-5}$ Pa s. The small viscosity also *a posteriori* justifies the fluid-like rheology assumption for the material in the vicinity of the band.

(g) Shear band displacement profiles at other V_0

To further test the validity of the Bingham model and band viscosity characteristics under different strain rates, additional imaging experiments were carried out at different V_0 conditions. The shear band displacement data for two other V_0 conditions, 0.3 and 1 mm s^{-1}, are shown in figure 13. Of these, we note that 0.3 mm s^{-1} was the critical velocity at which shear banding was first observed in Wood's metal at $\alpha = 0°$. In both cases (figure 13*a*,*c*), it can be seen that the displacement profiles evolve self-similarly, with the band thickness growing with time, similar to the previous observations made at $V_0 = 0.6$ mm s^{-1} (figure 11), indicating this to be a general characteristic of the shear band growth. The band thicknesses of about 26 µm (0.3 mm s^{-1}) and 35 µm (1 mm s^{-1}) are also comparable to that at 0.6 mm s^{-1}. Figure 13*b*,*d* shows the normalized displacement plots, where the experimental profiles are scaled using ν; the corresponding band viscosity is shown in the insets as before. At each V_0 condition, two streaklines across the band

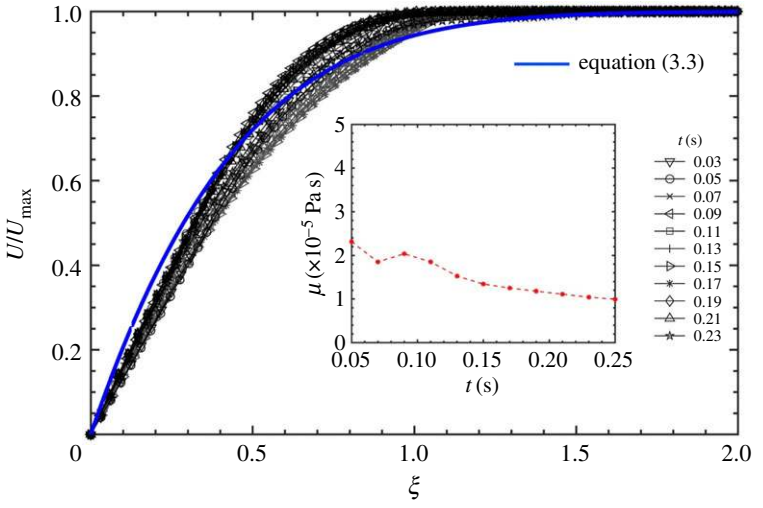

Figure 12. Normalized shear band displacement profiles from two different streaklines (black and grey) at different time instances of the sliding, plotted against $\xi = y/\sqrt{4\nu t}$. The experimental profiles are fitted using the adjustable parameter ν. They are seen to fall on a single curve, closely following the theoretical profile (solid blue line) predicted by the Bingham fluid model (equation (3.3)). The inset shows the shear band viscosity, μ. $V_0 = 0.6$ mm s^{-1}. (Online version in colour.)

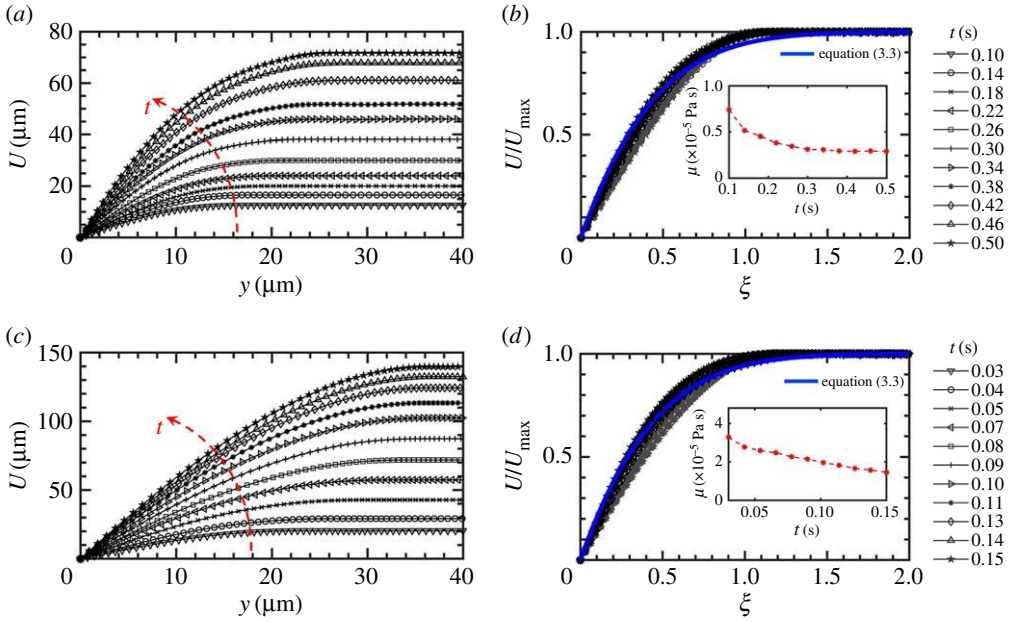

Figure 13. Shear band displacement data at $V_0 = 0.3$ mm s^{-1} (*a*, *b*) and $V_0 = 1$ mm s^{-1} (*c*, *d*). Plots (*a*,*c*) show the raw displacement data plotted against y at different t and (*b*,*d*) are the normalized displacement plots (U/U_{max} versus $\xi = y/\sqrt{4\nu t}$), where the shear band viscosity is also shown in the insets. (Online version in colour.)

were chosen for comparison with the model. Again, the model (equation (3.3)) appears to fit the data well in both cases. The agreement is slightly better at the lower speed (0.3 mm s^{-1}), where the band viscosity is also seen to remain constant during the shear banding process. At a higher V_0 of 1 mm s^{-1}, the band viscosity exhibits a slight drop. Note, however, that the viscosity values at different V_0 are all in the same 10^{-5} Pa s range.

In the above, we restricted ourselves to the analysis of shear band displacement results within the framework of an ideal Bingham fluid law with a linear rate dependence. Here, the primary goal has been to demonstrate the boundary layer growth during shear banding as a consequence of the fluid-like flow in the vicinity of the band, and to provide an order of magnitude estimate for the local viscosity. Nevertheless, it is quite likely that some perhaps weak power-law dependence (e.g. Herschel–Bulkley type) exists which our present model cannot capture. For the current flow geometry, self-similar solutions in general do not exist for a generalized non-Newtonian rheology [41], although the case of shear-thinning power-law fluids appears to have been solved by Bird [42] for specific exponents. Together with the direct measurements of the displacement fields, we hope this will provide a basis to explore a full Herschel–Bulkley-type model in the future.

4. Discussion

The experimental study with a low melting point alloy (Wood's metal) has reproduced all the essential features of shear banding in crystalline metals at low, approximately millimetre per second, speeds. Coupled with *in situ* imaging, this has enabled us to capture the dynamics of shear band nucleation and propagation, and time-resolved measurements of the plastic flow field around a developing shear band to be made at a high spatial resolution (approx. 1 µm). Inferences of the local shear band properties (band nucleation stress and dynamic viscosity) have been made at different strain rates. The observations pertaining to shear band onset at a critical stress and subsequent boundary layer-like (plastic) flow together support the Bingham-type description for the shear band.

(a) Critical stress criterion for shear band formation

Beginning with Zener [4,18], it is generally believed that shear banding is a consequence of loss of stability in the plastic flow due to temperature rise resulting from the deformation itself. That is, if the flow stress drop due to plastic heating is greater than the increase due to strain/strain-rate hardening, unstable flow will arise in a localized portion of the specimen as a shear band. This general idea has been successful in qualitatively explaining the prevalence of shear banding in metals under high strain rates (greater than $10^3\ \mathrm{s}^{-1}$) characterized by efficient plastic heating, and also under very low temperatures (less than 50 K), where, despite the low ambient temperature conditions, large temperature rises can still occur in the material due to the very small heat capacity value at cryogenic temperatures [43]. Therefore, an attempt was made to estimate the extent of temperature rise in the present case. Since we are concerned with the thermal conditions prevailing at the onset of the instability, we consider the temperature rise at the shear plane/zone (e.g. region *OA*, figure 1*a*) under the limiting case when the shear band has not yet formed and the flow is still homogeneous. Various analytical treatments, primarily based on Jaeger's moving heat-source solution [38], have been proposed for studying the shear zone temperatures in cutting. Here, we proceed in a manner similar to that of Loewen & Shaw [30]. In brief, we shall assume the chip–workpiece interface at the shear plane to be a 'sliding' contact, with chip and workpiece being the stationary and sliding members, respectively, and over which a constant heat flux $Q \sim \tau V_S$ is uniformly distributed; τ is the shear stress and V_S is the velocity component along the shear plane. The temperature solutions on both sides of the plane are obtained independently by assuming a portion of the heat leaves with the chip, while the remainder flows into the moving workpiece. As a last step, the unknown heat partitioning coefficient is obtained by using Blok's postulate [44] by matching the maximum temperatures on either side of the plane. While this procedure is approximate, the experimental results have been found to be in good agreement with the calculated temperatures [30]. For the present case ($V_0 \sim 0.3$–$8\ \mathrm{mm\ s}^{-1}$, $\alpha = 0^\circ$), where the characteristic Péclet number $Pe \sim V_0 t_0/\kappa \sim 10^{-3}$–$10^{-1} \ll 1$, the temperature solution reduces to

$$\Delta\theta = \frac{\sqrt{3}\kappa\varepsilon\tau V_0 t_0}{k(\kappa\sqrt{\pi} + V_0 t_0)}, \tag{4.1}$$

where $\Delta\theta$ is the temperature rise and ε is the strain right before shear band initiation, while other symbols have their usual meanings. The temperature rise $\Delta\theta$ is predicted at different V_0 by taking $\varepsilon \sim 0.5$ (from PIV), τ to be the same as $\tau_C \sim 70$ MPa, and room-temperature values for the thermophysical properties (table 1). These data are given in table 2. It can be seen that the temperature rise is no greater than 2 or 3°C over the entire range of V_0, indicating that temperature should have little effect on the shear banding instability. These temperature estimates have been also confirmed in our experiments, where a thermocouple was used to measure the temperature rise at three different locations: tool–chip contact, deformation zone and the free surface where workpiece material is transformed into a chip. Good agreement with the estimated temperatures (table 2) was found, with the maximum temperature rise (at tool–chip contact) being less than 4–5°C even at the highest cutting speed (8 mm s^{-1}). A more critical evaluation of the 'maximum load' criterion for shear band formation has been also made by considering the individual contributions to the flow stress, arising from strain, strain rate and temperature. These details are presented in appendix A, but it suffices to note here that the flow stress hardening term (due to rate effects) is always much greater (by two orders) than the temperature softening term, again suggesting weak thermal contribution to shear banding in the V_0 range investigated here. In addition to the thermal softening mechanism, several other fracture-type criteria [24] have been also proposed for shear band onset, including those based on critical plastic strain, stress intensity factor and J integral. However, these have not been supported by direct experimental observations. At a microstructural level, some postulated mechanisms for shear band initiation include those based on dynamic recrystallization [45–47], dislocation 'avalanche' mechanism [48–50], texture softening [51] and flow softening due to formation of microscopic voids.

In contrast to the above, our *in situ* observations of shear banding, together with force measurements, strongly suggest a simple stress-based criterion where macroscopic flow localization along a thin shear band sets in when the shear stress along the plane of maximum shear reaches a critical value τ_C. That τ_C remains constant over a range of V_0 (table 2) provides further support for this. As discussed earlier, the stress-based criterion for band formation explains the flow transition with increasing V_0 (figure 4). At low V_0 (less than or equal to 0.1 mm s^{-1}), because the shear flow stress is below τ_C (table 2), shear band formation is precluded and the flow remains homogeneous. Upon increasing V_0, because of the rate sensitivity, the flow stress is raised to τ_C, resulting in shear banding and associated flow localization. Furthermore, the picture of critical τ_C, or equivalently, critical strain rate since the flow stress depends only on the strain rate at large strains (figure 3*a*), is also consistent with the following several observations we have made during this study.

— As noted earlier, at $\alpha = 0°$, the homogeneous to shear banded flow transition occurred at about 0.3 mm s^{-1}. Experiments at different α showed that this critical transition speed actually increases with α : 0.4 mm s^{-1} for +20° and 1 mm s^{-1} for +40° [26]. This behaviour may be understood by noting that at a higher α (more positive), the strain imposed in the chip is smaller. Therefore, the V_0 required to reach the critical strain rate/shear stress necessary for shear band formation is correspondingly higher.
— Experiments performed at a higher t_0 of 500 µm at $\alpha = 0°$ showed that the critical V_0 for the flow transition increases to 1 mm s^{-1} (S.Y. and D.S. 2019, unpublished data). It is believed that this results from the fact that the shear zone thickness Δ, which determines the strain rate ($\dot{\varepsilon} = \varepsilon V_0/\Delta$), scales similarly with t_0 [30]. Therefore, again a higher V_0 must be needed to achieve the critical strain rate at which the τ_C condition for banding is satisfied.
— No shear banding was observed in our compression tests, consistent with the fact that the strain rates in compression are very small (10^{-5}–10^{-2} s^{-1}) and much below the critical strain rate (approx. 10 s^{-1}) required for band formation. According to our critical stress criterion, for the case of uniaxial compression, shear banding should be expected to occur when the shear stress on the plane of maximum shear (i.e. plane oriented at 45° with respect to the loading axis) reaches $\sigma/2$. From figure 3*a*, it may be seen that this value is much below the critical τ_C, more than by a factor of 2, under all testing conditions.

Lastly, we must mention that the constant shear stress criterion for banding is not limited to Wood's metal, but has been also confirmed in two other metal systems with different melting points (47 and 138°C). These results and dependence of τ_C on the material properties (melting point, for example) will be the subject of a separate publication.

(b) Boundary layer formation and fluid-like behaviour of shear band

The *in situ* study has enabled direct time-resolved measurements of the displacement and velocity profiles inside a developing shear band at high resolution. These observations have revealed, among other things, the self-similar temporal evolution of flow profiles during shear band growth; widening of the band thickness roughly as $t^{1/2}$; slow variation of the velocity and displacement field along the band length compared to across the thickness direction; and little dependence of the band growth dynamics on the external V_0 conditions. While such temporal evolution for the band growth, following the instability, has been postulated before [28,29], we believe our study provides the first direct experimental evidence. Furthermore, agreement between experimental data and the Bingham model has demonstrated viscous-like sliding near the shear band interface and provided a mechanism for shear band growth, based on momentum diffusion. Incidentally, this type of viscous sliding mechanism is known to be operative in metal interfaces also at a much smaller scale, for example, inside the slip bands [52] and near grain boundaries [53].

Given the low melting point of the alloy investigated in this study, a discussion of the generalizability of the flow observations to other systems is in order. Firstly, as noted earlier, the flow behaviour of this alloy at room temperature closely resembles that of conventional metals under high strain rates (more than $10^3\ s^{-1}$) where shear banding is typically observed—both in its constitutive form (high strain-rate dependence, high T_H, negligible strain hardening) as well as the flow phenomenology (homogeneous flow to shear banding transition with increasing strain rate). Secondly, recent evidence does show that the viscous sliding mechanism associated with banding is indeed a more general characteristic of polycrystalline metals. This result was established in our earlier studies [19,25] using post-mortem measurements of shear band displacement profiles in three different high-temperature alloys (pure Ti, Ti-6Al-4V alloy and Ni-base superalloy) and under high strain rates of 10^4–$10^5\ s^{-1}$, several orders higher than in the current study. The band viscosity in these metals was again found to be very small, however, in the mPa s range, suggesting some material dependence of this parameter. Given the vast difference in the strain rates and material properties between both the studies, the common observation of fluid-like behaviour of shear bands with a small viscosity is remarkable.

The above observations of similar shear band flow profiles across different material systems also make a case for continuum-level description of the band growth without the need for precise microstructure-level details. An effort to analytically study the spatio-temporal aspects of shear band flow, for instance, was made by Gioia & Ortiz [28]. Here, the extreme thinness of the bands, coupled with the fact that the field variation across the band thickness is much more rapid compared with other directions, was exploited to model shear band flow as a boundary layer problem. This facilitated analytical characterization of the boundary layer structure (shear band) in terms of velocity, plastic work and temperature fields. It follows from the theory that the velocity (and, consequently, displacement) profile around the band spreads out in time from an initial 'step' like profile, eventually approaching a steady state (see fig. 9 in [28]). Similarly, using boundary layer methods, DiLellio & Olmstead [29] have considered temporal evolution of a shear band and shown that the band first narrows down during the very initial stages of localization, which is followed by a growth stage characterized by an increase in the band thickness (as a power law with time) and attendant stress collapse. All these observations are in qualitative agreement with our shear band displacement field measurements, and are suggestive that shear banding belongs to the class of laminar plastic boundary layer problems [54]. Other solutions describing the spatial distribution of strain rate, velocity and temperature around a shear band include those by Wu & Freund [55] and Glimm *et al.* [56], although the viscoplastic law assumed

for the material is different in these studies. We hope that our time-resolved measurements of particle displacements and velocities in the neighbourhood of the shear band will help to validate (and extend) these analyses that are capable of incorporating all three effects (strain hardening/softening, rate hardening and thermal softening) into the constitutive law.

However, it is noteworthy that even with a simplified linear rate-dependent Bingham model, considerable insight is derived into the local flow character of the band and structural changes accompanying the instability. For example, a key finding from the analysis of experimental displacement results is the small material viscosity (10^{-3} to 10^{-5} Pa s) during the band growth that is indicative of the local fluid-like character of the shear band. This is in contrast to the flow behaviour of the starting material, characterized by the power-law relationship: $\sigma = K\dot{\varepsilon}^m$ (figure 3). The effective 'bulk' viscosity (μ_b) of this material may be estimated by writing σ as $\mu_b\dot{\varepsilon}$, where $\mu_b = K\dot{\varepsilon}^{1-m}$. Substituting the representative values for K and m, μ_b at typical shear band strain rates (10–100 s^{-1} for Wood's metal) is seen to fall in the 10^8 Pa s range, which is several orders of magnitude greater than the typical band viscosity. These main characteristics of shear banding—the onset of instability at a critical stress, followed by a large viscosity drop by several orders (more than 10) of magnitude—are reminiscent of the yield-stress fluids which behave in a solid-like manner (i.e. large viscosity value) below a critical yield stress, but flow as fluids above this stress. Akin to this 'solid to liquid' phase transition in yield-stress fluids, a breaking down of the microstructure at a critical stress (τ_C) may be also envisioned for the present case during shear band nucleation, which causes the material in the vicinity of the band to *flow* with little resistance during the subsequent growth phase. This picture of shear banding is also self-consistent with our choice of the Bingham constitutive law for the band in the first place.

Experimental examples of unsteady flow and boundary layer formation in ideal Bingham yield stress fluids under the flow geometry close to our case are rare, so a direct comparison of shear band profiles with that of actual fluids is not possible. However, the transient flow of a Herschel–Bulkley-type yield stress fluid (carbopol microgel) in a Couette cell has been shown to involve propagation of a plastic 'wave' (the boundary between the fluidized and non-fluidized regions) [57], similar to power-law shear band growth dynamics in the present case (figures 11 and 13). Similarly, the displacement and velocity profiles inside a yield stress fluid (two-dimensional) boundary layer, formed adjacent to a moving plate in a stationary fluid [58], are also in qualitative agreement with our observations.

5. Conclusion

In this study, a new experimental approach, using low melting point alloys, is developed to study the phenomenon of plastic flow localization in thin narrow layers—shear banding—at low speeds. Shear bands arise from an instability when a certain material plane loses its resistance to flow and thus accumulates large strains in its vicinity. Using *in situ* imaging, the dynamics of shear band nucleation, propagation and growth is characterized quantitatively. This has provided direct time-resolved measurements of the displacement and velocity profiles of the large strain plastic flow inside a shear band. Evolution of the shear band thickness roughly as a power law with time, analogous to boundary layer formation in fluids, is established using these measurements. A Bingham fluid model, formulated based on experimental observations, accurately captures the temporal evolution of shear band flow profiles and provides a mechanism for the band growth, based on momentum diffusion. The goal here has been to introduce a simple continuum-level model (with just one fitting parameter) that quantitatively predicts the shear band flow evolution and provides insight into the local flow character of the band, post the instability onset. The observations demonstrate fluid-like behaviour in the vicinity of the shear band, characterized by a very small viscosity. Coupled with the experimental result that shear band instability occurs at a critical stress, this casts a new perspective on shear banding as a 'solid-to-liquid'-type transition in yield-stress fluids, with the shear band itself being the boundary layer. It is believed that this picture of shear banding as a plastic boundary layer formation is common to a

range of crystalline metals. We regard this viewpoint as complementary to other analyses of shear localization phenomena in metals.

Data accessibility. The data supporting this paper are available as electronic supplementary material.
Competing interests. We declare we have no competing interests.
Funding. No funding has been received for this article.
Acknowledgements. D.S. acknowledges the faculty start-up support from the Department of Industrial and Systems Engineering and Texas A&M Engineering Experiment Station.

Appendix A

We carry out a critical evaluation of the well-known 'maximum' load criterion for predicting the shear band onset, originally proposed by Zener [18] and later extended by others [12]. According to this criterion, the homogeneous plastic flow will be no longer stable when the stress–strain curve of a material develops a negative slope. For a general flow stress function $\sigma = f(\varepsilon, \dot{\varepsilon}, \theta)$, the critical condition for the instability is

$$\frac{\mathrm{d}\sigma}{\mathrm{d}\varepsilon} = \left(\frac{\partial\sigma}{\partial\varepsilon}\right)_{\dot{\varepsilon},\theta} + \left(\frac{\partial\sigma}{\partial\dot{\varepsilon}}\right)_{\varepsilon,\theta}\frac{\mathrm{d}\dot{\varepsilon}}{\mathrm{d}\varepsilon} + \left(\frac{\partial\sigma}{\partial\theta}\right)_{\varepsilon,\dot{\varepsilon}}\frac{\mathrm{d}\theta}{\mathrm{d}\varepsilon} \leq 0, \tag{A 1}$$

where θ is the temperature. We perform an order-of-magnitude analysis of the individual terms in the above equation. Given that the temperature rise in the velocity range of interest is small (table 2), we evaluate these terms at $\theta \sim 23^{\circ}\mathrm{C}$. Earlier, we have noted that the strain (within the matrix/segment) at which shear bands initiate is about 0.5. Given that the slope of the stress–strain curve at this strain level is ≈ 0 (figure 3*a*) at all strain rates, the first term $(\partial\sigma/\partial\varepsilon)_{\dot{\varepsilon},\theta}$ can be safely assumed to be zero.

Also, from figure 3*b*, we have seen that the flow stress (in MPa) at any given strain can be represented as $K\dot{\varepsilon}^m$, with m being in the range of 0.13–0.17 and K showing little variation with ε. Coupled with the fact that the nominal strain rate in cutting can be given by $\varepsilon V_0/\Delta$ (where the shear zone thickness Δ is about 50 µm), the second term as a whole can be written as $Km\varepsilon^{m-1}(V_0/\Delta)^m$. Substituting the representative values, the second term in equation (A 1) is seen to fall in the 30–72 MPa range, depending on V_0 (0.3–8 mm s^{-1}).

Lastly, we estimate the last term by obtaining $\mathrm{d}\theta/\mathrm{d}\varepsilon$ from equation (4.1), while the $(\partial\sigma/\partial\theta)_{\varepsilon,\dot{\varepsilon}}$ term is obtained from the literature (due to lack of data for Wood's metal). Since $\partial\sigma/\partial\theta$ for various low melting point alloys ($T_m < 220^{\circ}\mathrm{C}$) is found to lie between $-1/7$ and $-1/3$ MPa $^{\circ}\mathrm{C}^{-1}$ [59,60], a value of $-1/6$ MPa $^{\circ}\mathrm{C}^{-1}$ is used for the present calculations. Putting together these values gives an estimate for the third (flow softening) term in equation (A 1) in the range of -0.04 to -0.9 MPa. Note that precise choice for the $\partial\sigma/\partial\theta$ value does not introduce a large error in the calculation. Importantly, this shows that the thermal softening term is much smaller than the strain-rate hardening term, by about two orders of magnitude, under conditions where shear bands were experimentally observed. These observations suggest that a re-assessment of the (commonly used) maximum load criterion for shear band formation is in order.

References

1. Poirier JP. 1980 Shear localization and shear instability in materials in the ductile field. *J. Struct. Geol.* **2**, 135–142. (doi:10.1016/0191-8141(80)90043-7)
2. Bowden PB, Raha S. 1970 The formation of micro shear bands in polystyrene and polymethylmethacrylate. *Philos. Mag.* **22**, 463–482. (doi:10.1080/14786437008225837)
3. Winter RE. 1975 Adiabatic shear of titanium and polymethylmethacrylate. *Philos. Mag.* **31**, 765–773. (doi:10.1080/14786437508229629)
4. Zener C. 1948 The micro-mechanism of fracture. In *Fracturing of metals* (eds F Jonassen, WP Roop, RT Bayless), pp. 3–31. Cleveland, OH: American Society for Metals.
5. Rice JR. 1976 The localization of plastic deformation. In *Proc. 14th Int. Congress on Theoretical and Applied Mechanics* (ed. WT Koiter), pp. 207–220. Amsterdam, The Netherlands: North-Holland.

6. Donovan PE, Stobbs WM. 1981 The structure of shear bands in metallic glasses. *Acta Metall.* **29**, 1419–1436. (doi:10.1016/0001-6160(81)90177-2)
7. Lewandowski JJ, Greer AL. 2006 Temperature rise at shear bands in metallic glasses. *Nat. Mater.* **5**, 15–18. (doi:10.1038/nmat1536)
8. Dodd B, Bai Y. 2012 *Adiabatic shear localization: frontiers and advances*, 2nd edn. Amsterdam, The Netherlands: Elsevier.
9. Dodd B, Walley SM, Yang R, Nesterenko VF. 2015 Major steps in the discovery of adiabatic shear bands. *Metall. Mater. Trans. A* **46**, 4454–4458. (doi:10.1007/s11661-015-2739-1)
10. Hatherly M, Malin AS. 1984 Shear bands in deformed metals. *Scr. Metall.* **18**, 449–454. (doi:10.1016/0036-9748(84)90419-8)
11. Backofen WA. 1972 *Deformation processing*, p. 255. Reading, MA: Addison-Wesley.
12. Recht RF. 1964 Catastrophic thermoplastic shear. *J. Appl. Mech.* **31**, 186–193. (doi:10.1115/1.3629585)
13. Hutchings IM, Winter RE, Field JE. 1976 Solid particle erosion of metals: the removal of surface material by spherical projectiles. *Proc. R. Soc. Lond. A* **348**, 379–392. (doi:10.1098/rspa.1976.0044)
14. Wright TW. 2002 *The physics and mathematics of adiabatic shear bands*. Cambridge Monographs on Mechanics. Cambridge, UK: Cambridge University Press.
15. Walley SM. 2007 Shear localization: a historical overview. *Metall. Mater. Trans. A* **38**, 2629–2654. (doi:10.1007/s11661-007-9271-x)
16. Walley SM. 2012 Strain localization in energetic and inert granular materials. In *Adiabatic shear localization: frontiers and advances* (eds B Dodd, Y Bai), pp. 267–310. Amsterdam, The Netherlands: Elsevier.
17. Timothy SP, Hutchings IM. 1985 The structure of adiabatic shear bands in a titanium alloy. *Acta Metall.* **33**, 667–676. (doi:10.1016/0001-6160(85)90030-6)
18. Zener C, Hollomon JH. 1944 Effect of strain rate upon plastic flow of steel. *J. Appl. Phys.* **15**, 22–32. (doi:10.1063/1.1707363)
19. Sagapuram D, Viswanathan K, Trumble KP, Chandrasekar S. 2018 A common mechanism for evolution of single shear bands in large-strain deformation of metals. *Philos. Mag.* **98**, 3267–3299. (doi:10.1080/14786435.2018.1524586)
20. Giovanola JH. 1988 Adiabatic shear banding under pure shear loading. Part I. Direct observation of strain localization and energy dissipation measurements. *Mech. Mater.* **7**, 59–71. (doi:10.1016/0167-6636(88)90006-3)
21. Zhou M, Rosakis AJ, Ravichandran G. 1996 Dynamically propagating shear bands in impact-loaded prenotched plates. I. Experimental investigations of temperature signatures and propagation speed. *J. Mech. Phys. Solids* **44**, 981–1006. (doi:10.1016/0022-5096(96)00003-8)
22. Marchand A, Duffy J. 1988 An experimental study of the formation process of adiabatic shear bands in a structural steel. *J. Mech. Phys. Solids* **36**, 251–283. (doi:10.1016/0022-5096(88)90012-9)
23. Duffy J, Chi YC. 1992 On the measurement of local strain and temperature during the formation of adiabatic shear bands. *Mater. Sci. Eng. A* **157**, 195–210. (doi:10.1016/0921-5093(92)90026-W)
24. Guduru PR, Rosakis AJ, Ravichandran G. 2001 Dynamic shear bands: an investigation using high speed optical and infrared diagnostics. *Mech. Mater.* **33**, 371–402. (doi:10.1016/S0167-6636(01)00051-5)
25. Sagapuram D, Viswanathan K. 2018 Evidence for Bingham plastic boundary layers in shear banding of metals. *Extreme Mech. Lett.* **25**, 27–36. (doi:10.1016/j.eml.2018.10.002)
26. Yadav S, Sagapuram D. 2019 Nucleation and boundary layer growth of shear bands in machining. *J. Manuf. Sci. Eng.* **141**, 1–16. (doi:10.1115/1.4044103)
27. Yadav S, Feng G, Sagapuram D. 2019 Dynamics of shear band instabilities in cutting of metals. *CIRP Ann.* **68**, 45–48. (doi:10.1016/j.cirp.2019.04.030)
28. Gioia G, Ortiz M. 1996 The two-dimensional structure of dynamic boundary layers and shear bands in thermoviscoplastic solids. *J. Mech. Phys. Solids* **44**, 251–292. (doi:10.1016/0022-5096(95)00071-2)
29. DiLellio JA, Olmstead WE. 1997 Temporal evolution of shear band thickness. *J. Mech. Phys. Solids* **45**, 345–359. (doi:10.1016/S0022-5096(96)00098-1)
30. Shaw MC. 1989 *Metal cutting principles*. Oxford, UK: Oxford University Press.

31. Sagapuram D, Viswanathan K, Mahato A, Sundaram NK, M'Saoubi R, Trumble KP, Chandrasekar S. 2016 Geometric flow control of shear bands by suppression of viscous sliding. *Proc. R. Soc. A* **472**, 20160167. (doi:10.1098/rspa.2016.0167)
32. Guo Y, Compton WD, Chandrasekar S. 2015 *In situ* analysis of flow dynamics and deformation fields in cutting and sliding of metals. *Proc. R. Soc. A* **471**, 20150194. (doi:10.1098/rspa.2015.0194)
33. Adrian RJ, Westerweel J. 2010 *Particle image velocimetry*. Cambridge, UK: Cambridge University Press.
34. Klopp RW, Clifton RJ, Shawki TG. 1985 Pressure-shear impact and the dynamic viscoplastic response of metals. *Mech. Mater.* **4**, 375–385. (doi:10.1016/0167-6636(85)90033-X)
35. Tong W, Clifton RJ, Huang S. 1992 Pressure-shear impact investigation of strain rate history effects in oxygen-free high-conductivity copper. *J. Mech. Phys. Solids* **40**, 1251–1294. (doi:10.1016/0022-5096(92)90015-T)
36. Childs THC. 2014 Adiabatic shearing in metal machining. In *CIRP encyclopedia of production engineering* (eds L Laperriï£¡re, G Reinhart), pp. 27–33. Berlin, Germany: Springer.
37. Schlichting H. 1955 *Boundary-layer theory*, 1st edn. New York, NY: McGraw-Hill.
38. Carslaw HS, Jaeger JC. 1959 *Conduction of heat in solids*, 2nd edn. London, UK: Oxford University Press.
39. Pascal H. 1989 Propagation of disturbances in a non-Newtonian fluid. *Physica D* **39**, 262–266. (doi:10.1016/0167-2789(89)90008-0)
40. Huilgol RR. 2004 On kinematic conditions affecting the existence and non-existence of a moving yield surface in unsteady unidirectional flows of Bingham fluids. *J. Non-Newtonian Fluid Mech.* **123**, 215–221. (doi:10.1016/j.jnnfm.2004.08.009)
41. Duffy BR, Pritchard D, Wilson SK. 2014 The shear-driven Rayleigh problem for generalised Newtonian fluids. *J. Non-Newtonian Fluid Mech.* **206**, 11–17. (doi:10.1016/j.jnnfm.2014.02.001)
42. Bird RB. 1959 Unsteady pseudoplastic flow near a moving wall. *AlChE J.* **5**, 565–6D. (doi:10.1002/aic.690050429)
43. Basinski ZS. 1957 The instability of plastic flow of metals at very low temperatures. *Proc. R. Soc. Lond. A* **240**, 229–242. (doi:10.1098/rspa.1957.0079)
44. Blok H. 1937 Theoretical study of temperature rise at surface of actual contact under oiliness lubricating conditions. In *Proc. General Discussion on Lubrication & Lubricants*, vol. 2, pp. 222–235. London, UK: Institution of Mechanical Engineers.
45. Meyers MA, Lasalvia JC, Nesterenko VF, Chen YJ, Kad BK. 1996 Dynamic recrystallization in high strain rate deformation. In *Proc. 3rd Int. Conf. on Recrystallization and Related Phenomena, Monterey, CA, USA, 21–24 October 1996*, pp. 279–286.
46. Landau P, Osovski S, Venkert A, Gärtnerová V, Rittel D. 2016 The genesis of adiabatic shear bands. *Sci. Rep.* **6**, 37226. (doi:10.1038/srep37226)
47. Rodríguez-Martínez JA, Vadillo G, Rittel D, Zaera R, Fernández-Sáez J. 2015 Dynamic recrystallization and adiabatic shear localization. *Mech. Mater.* **81**, 41–55. (doi:10.1016/j.mechmat.2014.10.001)
48. Gilman JJ. 1994 Micromechanics of shear banding. *Mech. Mater.* **17**, 83–96. (doi:10.1016/0167-6636(94)90051-5)
49. Nabarro FRN. 1967 *Theory of crystal dislocations*. Mineola, NY: Dover Publications Inc.
50. Antolovich SD, Armstrong RW. 2014 Plastic strain localization in metals: origins and consequences. *Prog. Mater. Sci.* **59**, 1–160. (doi:10.1016/j.pmatsci.2013.06.001)
51. Dillamore IL, Roberts JG, Bush AC. 1979 Occurrence of shear bands in heavily rolled cubic metals. *Metal Sci.* **13**, 73–77. (doi:10.1179/msc.1979.13.2.73)
52. Zener C. 1948 *Elasticity and anelasticity of metals*. Chicago, IL: University of Chicago Press.
53. Giannuzzi LA, King AH. 1985 Grain boundary viscosity at high temperature and the grain boundary phase transformation. *Scr. Metall.* **19**, 291–294. (doi:10.1016/0036-9748(85)90316-3)
54. Oldroyd JG. 1947 Two-dimensional plastic flow of a Bingham solid: a plastic boundary-layer theory for slow motion. *Math. Proc. Cambridge Philos. Soc.* **43**, 383–395. (doi:10.1017/S0305004100023616)
55. Wu FH, Freund LB. 1984 Deformation trapping due to thermoplastic instability in one-dimensional wave propagation. *J. Mech. Phys. Solids* **32**, 119–132. (doi:10.1016/0022-5096(84)90014-0)
56. Glimm JG, Plohr BJ, Sharp DH. 1996 Tracking of shear bands. I. The one-dimensional case. *Mech. Mater.* **24**, 31–41. (doi:10.1016/0167-6636(96)00029-4)

57. Divoux T, Tamarii D, Barentin C, Teitel S, Manneville S. 2012 Yielding dynamics of a Herschel–Bulkley fluid: a critical-like fluidization behaviour. *Soft Matter* **8**, 4151–4164. (doi:10.1039/c2sm06918k)
58. Boujlel J, Maillard M, Lindner A, Ovarlez G, Chateau X, Coussot P. 2012 Boundary layer in pastes—displacement of a long object through a yield stress fluid. *J. Rheol.* **56**, 1083–1108. (doi:10.1122/1.4720387)
59. Pei M, Qu J. 2005 Constitutive modeling of lead-free solders. In *ASME 2005 Pacific Rim Technical Conf. and Exhibition on Integration and Packaging of MEMS, NEMS, and Electronic Systems collocated with the ASME 2005 Heat Transfer Summer Conf.*, pp. 1307–1311. New York, NY: American Society of Mechanical Engineers.
60. Shi XQ, Zhou W, Pang HLJ, Wang ZP, Wang YP. 1999 Effect of temperature and strain rate on mechanical properties of 63Sn/37Pb solder alloy. *ASME J. Elect. Packaging* **121**, 179–185. (doi:10.1115/1.2792681)